OXFORD Regenerative Biomaterials

Regenerative Biomaterials, 2024, **11**, rbad111
https://doi.org/10.1093/rb/rbad111
Advance Access Publication Date: 21 December 2023
Research article

Fibrous topology promoted pBMP2-activated matrix on titanium implants boost osseointegration

Ting He[1], Yichun Wang[1], Ruohan Wang[1], Huan Yang[1], Xueyi Hu[1], Yiyao Pu[1], Binbin Yang[1,2], Jingyuan Zhang[1], Juan Li[3,*], Chongxiang Huang[1,4], Rongrong Jin[1,*], Yu Nie [1,*] and Xingdong Zhang[1]

[1]National Engineering Research Centre for Biomaterials/College of Biomedical Engineering, Sichuan University, Chengdu 610064, China
[2]Department of the Affiliated Stomatological Hospital of Southwest Medical University, Southwest Medical University, Luzhou 646000, China
[3]State Key Laboratory of Oral Diseases, West China School of Stomatology, West China Hospital of Stomatology, Sichuan University, Chengdu 610041, China
[4]School of Aeronautics and Astronautics, Sichuan University, Chengdu 610064, China

*Correspondence address. E-mail: nie_yu@scu.edu.cn (Y.N.); jinrr2015@scu.edu.cn (R.J.); lijuan@scu.edu.cn (J.L.)

Abstract

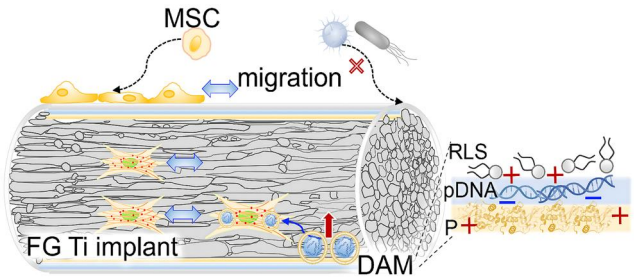

Titanium (Ti) implants have been extensively used after surgical operations. Its surface bioactivity is of importance to facilitate integration with surrounding bone tissue, and ultimately ensure stability and long-term functionality of the implant. The plasmid DNA-activated matrix (DAM) coating on the surface could benefit osseointegration but is still trapped by poor transfection for further application, especially on the bone marrow mesenchymal stem cells (BMSCs) *in vivo* practical conditions. Herein, we constructed a DAM on the surface of fibrous-grained titanium (FG Ti) composed of phase-transition lysozyme (P) as adhesive, cationic arginine-rich lipid (RLS) as the transfection agent and plasmid DNA (pDNA) for bone morphology protein 2 (BMP2) expression. The cationic lipid RLS improved up to 30-fold higher transfection than that of commercial reagents (Lipofectamine 2000 and polyethyleneimine) on MSC. And importantly, Ti surface topology not only promotes the DAM to achieve high transfection efficiency (~75.7% positive cells) on MSC due to the favorable combination but also reserves its contact induction effect for osteoblasts. Upon further exploration, the fibrous topology on FG Ti could boost pDNA uptake for gene transfection, and cell migration in MSC through cytoskeleton remodeling and induce contact guidance for enhanced osteointegration. At the same time, the cationic RLS together with adhesive P were both antibacterial, showing up to 90% inhibition rate against *Escherichia coli* and *Staphylococcus aureus* with reduced adherent microorganisms and disrupted bacteria. Finally, the FG Ti-P/pBMP2 implant achieved accelerated bone healing capacities through highly efficient gene delivery, aligned surface topological structure and increased antimicrobial properties in a rat femoral condylar defect model.

Keywords: plasmid DNA-activated matrix; aligned surface topology; antibacterial activity; osseointegration

Introduction

The slowly integrated interface often causes loosening and detachment of titanium (Ti) implants, thus troubling dental and orthopedic healing post-operations [1, 2]. It is relatively difficult for the surrounding cell to adhere to the bioinert surface of Ti. Therefore, a more bioactive surface is demanded to benefit early and rapid osseointegration.

Various interface modifications have been applied in implants to improve bioactivity, especially the widely used protein coatings with biological functions [3–6]. However, the short half-life and the supraphysiological coating doses of protein still hampered the practical application due to the potential prolonged hazardous responses [5]. As an alternative, gene-activated matrix (GAM) coating incorporated with osteogenic genes (such as pBMP2 [7, 8], miRNA [9, 10], and siCkip-1 [11]) highly improved osseointegration of implants due to prolonged transgene activity and better immune compatibility. Unfortunately, the poor delivery efficiency on the hard-to-transfect targeting cells caused by the helpless delivery vector, limited gene loading and uncontrolled release is still blocked in preclinical studies [12]. More importantly, the interaction between carrier system and implant biophysical cues was rarely explored, especially for further application *in vivo* practical conditions. Nevertheless, screening efficient osteoinductive gene/non-viral vectors [9, 13], increasing the thickness of the coating [14] and changing loading strategies [15] can ameliorate the situation to a certain extent. Apart from this, micropattern topological structure modification (the roughness, width and depth) [16] has been documented as a useful physical technique, enabling an augmented specific surface area for enhanced DNA loading capacity [10] and inducing directional adhesion and migration of osteoblasts to accelerate the osseointegration process [17]. More interestingly, surface patterning also

Received: 30 October 2023. **Revised:** 25 November 2023. **Accepted:** 4 December 2023

potentially promotes gene transfection by controlling cell adhesion, spreading, and morphology mediated by cytoskeleton remodeling [18–21]. Therefore, it becomes imperative to develop an optimal equilibrium or a more ingenious system that can effectively achieve high gene transfection by favorable surface topology.

In addition to focusing on the promotion of osteogenic activity by surface modifications, the problem of bacterial infection should not be overlooked. Infections at the implant interface can lead to implant loosening and detachment [22, 23]. While designing surfaces with antimicrobial capabilities is essential, some antibacterial agents may inhibit osteoblast cell growth or interfere with effective biochemical molecules. Increasing the thickness of antibacterial coatings for improved antimicrobial activity can also potentially cover beneficial surface topologies conducive to osteogenic differentiation and gene transfection [24, 25]. Hence, it is particularly important to develop a more ingenious implant system that can efficiently inhibit bacteria growth while allowing sufficient osteoblast growth by the favorable integration of specific topologic structure and GAM modification.

Herein, we construct a plasmid DNA-activated matrix (DAM) coating based on our previously fabricated fibrous-grained titanium (FG Ti) [26, 27], which was used to modulate the cytoskeleton of MSC, to maximize the biological activity for better osseointegration. The DAM consisted of phase-transition lysozyme (P), cationic lipids (RLS) and plasmid BMP2, assembled using layer-by-layer (LBL) coating technology. Among them, the P acts as an advanced adhesive with broad-spectrum antimicrobial activity [28]. The RLS with arginine-rich periphery simultaneously guarantees high gene transfection efficiency and facilitates bacteriostasis [29–31]. The physical surface topology of FG Ti and the DAM components synergize, enabling the FG Ti-P/pDNA-6 implant to promote bone integration through efficient gene delivery, an aligned fibrous texture and antibacterial properties. The study includes an exploration of transgene efficiency, antimicrobial activity, related interaction mechanisms and an *in vivo* osteointegration evaluation using a rat femoral condyle defect model.

Materials and methods

Materials

Commercially pure Ti (ASTM Grade 2) was provided by the Baoji Titanium Industry Company (China). In this work, coarse-grained titanium (CG Ti) and FG Ti were used with CG Ti acting as the control. CG Ti was produced by vacuum annealing commercial pure Ti. FG Ti was a high-strength pure Ti with aligned bone-mimicking fibrous grains, obtained by extruding, rotary swaging and annealing CG Ti, which has been thoroughly characterized in our previous study [26]. Cationic lipid (RLS) was synthesized in our group as described previously [30]. Lipofectamine 2000 (Lipo 2000), a plasmid encoding enhanced green fluorescent proteins (pEGFP) and luciferase encoding plasmid (pGL3) were from Invitrogen (USA). Lysozyme (from hen egg white), tris (2-carboxyethyl) phosphine (TCEP), branched polyethyleneimine (PEI, 25 kDa), Alizarin Red S (ARS), rhodamine-phalloidin, 4,6-diamino-2-phenyl indole (DAPI) and the chemical dimethyl sulfoxide were obtained from Sigma-Aldrich Company (USA). The quartz crystals coated with gold were purchased from Biolin Scientific (Sweden). Silicon wafers were obtained from Zhejiang Lijing Optoelectronic Technology (China). A poly lactic acid sheet with biodegradable properties (PLA) was supplied by Sichuan XingTai Pule Medical Equipment Co., Ltd (China). Acetone and absolute ethyl alcohol were from Aladdin (Shanghai, China). The N-2-hydroxyethylpiperazine-N-ethane-sulphonicacid (HEPES) buffer, 4% paraformaldehyde, Triton X-100, fluorescein isothiocyanate (FITC)-labeled phalloidin, tetracycline hydrochloride ($C_{22}H_{24}N_2O_8$·HCl, TE), calcein (CA) and toluidine blue were from Solarbio (China). The bone morphogenetic protein-2 (BMP2) gene carried by the plasmid of pcDNA3.1 (pBMP2) was constructed by Sangon Biotech (China). The plasmids were expanded in *Escherichia coli*. To purify the plasmids, a commercial plasmid purification kit (Qiagen, Germany) was used. Glutaraldehyde was provided by the Lilai Biomedicine Experiment Center (China). Uranyl acetate was purchased from SPI-Chem (USA). Lead citrate was from Delta (China). The following chemicals including concentrated nitric acid (HNO_3), hydrofluoric acid (HF), concentrated hydrochloric acid (HCl) and hydrogen peroxide were obtained from Sichuan Kelun Pharmaceutical Co., Ltd (China).

Mouse osteoblast progenitor cells (MC3T3-E1) were derived from a library of the Chinese Academy of Science Cell Bank. Bone marrow mesenchymal stem cells (BMSCs) were extracted from 5 to 7-day-old female neonatal Sprague Dawley (SD) rats. The Australian fetal bovine serum (FBS) and minimum essential medium Alpha (α-MEM) were procured from Life Technologies Corporation (USA). Label IT® tracker™ intracellular nucleic acid Localization kits were obtained from Mirusbio (USA). The Ori-Cell Counting Kit-8 kit (CCK-8) was obtained from Oriscience (China). The PicoGreen dsDNA quantitation kit was purchased from Yeasen (China). Cell Tracker™ Green CMFDA was from Thermo (USA). Reagents related to the Trizol reagent kit, iScript cDNA synthesis kit and iQ SYBR green supermix were procured from Accurate Biology as commercially accessible products (China). The primers for quantitative reverse transcription PCR of rat osteogenesis were synthesized from Tsingke Biotechnology Co., Ltd (China), as listed in Supplementary Table S1. A 5 × loading buffer was from Cell Signal Technology (USA). Antibodies against BMP2 were from Abcam (UK). Antibodies against β-actin, goat anti-rabbit IgG-HRP antibody, radio-immunoprecipitation assay lysis buffer (RIPA), glycine, phosphate buffer saline (PBS) solution, BCA protein quantitation kit, western blot (WB) primary antibody diluent and western blocking solution were obtained from Beyotime (China). Phenylmethylsulfonyl fluoride protease inhibitor, Clarity™ western enhanced chemiluminescence substrate kit and sodium dodecyl sulfate-polyacrylamide gel electrophoresis gel rapid preparation kit were available from Bio-Rad (USA). *Staphylococcus aureus* (ATCC292133) and *E.coli* (ATCC8739) came from the American Type Culture Collection (USA).

All female SD rats provided by Chengdu Dossy Experimental Animals Co., Ltd were used in this study (China). Enrofloxacin ($C_{19}H_{22}FN_3O_3$) and pentobarbital sodium ($C_{11}H_{17}O_3N_2Na$) were obtained from Ailu Biological Tech Co., Ltd (China). Ethylenediamine tetraacetic acid decalcified solution was from Biosharp (China).

Titanium substrate preparation and phase-transition lysozyme (P) coating

FG Ti and CG Ti were machined as reported previously [26]. The machined FG Ti and CG Ti were then cut into discs (8.0 × 8.0 mm, 1.5 mm thick) and processed into FG Ti rods with a diameter of 2.0 mm and a length of 4.0 mm. Subsequently, all samples underwent successive washes with acetone, ethanol and deionized water in that order. They were sequentially polished by carborundum papers with different grits, and cleaned in a solution (HNO_3, 6.0%; HF, 7.5%; and deionized water, 86.5%; v/v) for 1 min at 25°C. Lastly, all discs and rods were thoroughly

ultrasonically cleaned in deionized water, dehydrated with ethanol and dried at 110–120°C for 30 min.

Followingly, P was coated onto the Ti slices/rods or silicon wafers as the adhesive. Ti slices/rods or silicon wafers were immersed in a solution of mixed HEPES buffer (10 mmol/l) consisting of lysozyme (5.0 mg/ml) and TCEP (50 mmol/l) and incubated for 2 h at an equal volume. After removal of the solution, the Ti slices/rods or silicon wafers were instantly rinsed with deionized water to eliminate salts and other additives and dried under nitrogen to obtain P-coated Ti.

Construction of pDNA-activated matrix

Multilayered pDNA coatings were formed through the layer-by-layer assembly method, as explained by Decher *et al.* [32, 33]. First, cationic RLS was synthesized according to our earlier research [29], and the molecular structure was characterized by ^{1}H-NMR and MALDI-TOF-MS. Subsequently, the assemblies (1 mg/ml) were prepared by an injection method [29], and pDNA (100 μg/ml) was prepared in HBG buffer (5% glucose in HEPES buffer, w/v, pH 7.4). Then, the P-coated Ti was alternately immersed into pDNA and RLS solution for 20 min to build up $(pDNA/RLS)_n$ (n represents the number of bilayers) films. At every interval, Ti discs/rods or silicon wafers were rinsed with deionized water to remove unbound pDNA or RLS from the surface. The process was repeated six times, and after the final rinse step, DAM-coated substrates were dried under nitrogen and kept in the desiccator.

Microstructural characterization

Surface topography

The surface microstructure morphology of the Ti/silicon wafers before and after decoration was accessed by field-emission scanning electron microscopy (FE-SEM, S-4800, Hitachi), and a beam voltage of 15 kV was used. All Ti sheets were sputtered with gold before the FE-SEM examination. The roughness of the DAM coating was investigated by atomic force microscopy (AFM, afm$^+$, Bruker) with the tapping mode. Subsequently, the roughness was analyzed by the NanoScope Analysis software (Bruker, ver 2.0).

Young's modulus of the DAM films on the Ti surface was characterized by AFM. Three different locations for each sample were measured by a cantilever that had a noted spring constant of 0.4086 N/m. The Sneddon model was used as the modulus fitting model with a range of 30–90%, and the data were analyzed by NanoScope Analysis software.

Water contact angle measurements

The water contact angles of the pristine and decorated Ti substrates were measured using a theta lite optical tensiometer (TL, Theta Lite, Biolin Scientific). The tip of the syringe was filled with water and cautiously dropped onto the surface of FG Ti discs parallelly and vertically to the rolling direction (RD) and CG Ti discs (the control group). An image of the drop shape formed on the surface was captured by the camera and the contact angle was obtained automatically using the Young–Laplace fit equation with the One Attention software provided by the manufacturer, where parallel tests were carried out on three non-overlapping areas-based FG Ti parallelly and vertically to the RD and CG Ti arbitrarily.

Surface zeta potential

P and DAM coating were decorated on the PLA (1.0 cm × 2.0 cm) as the same method described in the Titanium substrate preparation and phase-transition lysozyme (P) coating and Construction of pDNA-activated matrix (DAM) sections. After every layer deposition, surface zeta (ζ) potential changes in real-time were measured in a potassium chloride solution (0.1 mol/l) at pH 7.4 by an electrokinetic analyzer for solid surface analysis (SurPASS3, Anton Paar) with a regulated gap cell.

X-ray photoelectron spectroscopy

The fundamental makeup of multilayered DAM films modified Ti substrate was examined using X-ray photoelectron spectroscopy (XPS, K-Alpha, Thermo Scientific). The XPS spectra were meticulously calibrated by C 1s peak position (284.8 eV).

The loading of pDNA in $(pDNA/RLS)_n$ film

The loading of pDNA embedded in DAM was determined after every pDNA/RLS bilayer deposition on silicon wafers using an ultraviolet-visible spectrophotometer (UV-vis, Lambda 850, PerkinElmer) in diffuse reflectance mode after baseline calibration with blank wafers, with a wavelength between 200 and 800 nm. Before drawing a diagram, the reflectance was converted to absorbance.

Quartz crystal microbalance with dissipation assay

The stepwise deposition process of pDNA and RLS was observed timely using the quartz crystal microbalance with dissipation assay (QCM-D, Qsense Analyzer, Biolin Scientific). Firstly, P-coating was prepared on an Aurum (Au)-coated quartz crystal as the same method described in the Titanium substrate preparation and phase-transition lysozyme (P) coating section. Then it was installed in the test cell of the instrument and washed thoroughly with ultrapure (UP) water to obtain a stable baseline. Afterward, the configured pDNA solution (100 μg/ml) and RLS solution (1.0 mg/ml) were pumped into the channel alternatively at a controlled flux speed of 30 μl/min. At each change interval, the unbound polyelectrolyte on the substrate was thoroughly rinsed with UP water for 3–5 min. The deposition process was repeated for six cycles. The growth behavior of multilayer coatings was monitored by recording frequency/dissipation-time curves. Finally, the mass and thickness of the deposited $(pDNA/RLS)_6$ films were quantified using Dfind Smartfit modeling in the affiliated Dfind software from Q-Sense.

Variable angle spectroscopic ellipsometry measurements

Variable angle spectroscopic ellipsometry (VASE, SENpro, SENTECH) was used to verify the thickness of films in the dry state. Before the test, the P layer was first deposited onto the surface of silicon wafers as a precursor and blown dry under nitrogen. The thickness of DAM film (one and six bilayers) was measured with a continuous wavelength from 370 to 1050 nm and calculated according to the Cauchy model.

The stability of six bilayer DAM films under physiological conditions

The stability of coatings was determined by the PicoGreen dsDNA kit. Firstly, the standard curve was drawn at different concentration gradients according to the reagent manual. The specimen with six bilayer DAM films was immersed in DNase-free PBS (pH 7.4). At pre-determined time points (0, 0.5, 1, 2, 3, 7 and 14-day), the free pDNA in the supernatant was collected and replaced with equal volume fresh PBS buffer. The collected free pDNA was stained with the PicoGreen and monitored by the microplate reader (Synergy^{TM} H1, BioTek) with an excitation/emission wavelength of 480/520 nm. Finally, the remaining pDNA content was calculated.

Gene transfection and osteogenesis of DAM-coated Ti *in vitro*

Cell culture

In vitro studies were carried out on MC3T3-E1 and BMSCs. BMSCs derived from 5 to 7-day-old SD rats were procured. Specifically, the femur and tibia of the rats were isolated f in a sterile environment and the muscle was removed from the surface of the bones. Afterward, the treated femur and tibia were saturated in 75% ethanol for 30 s and subsequently placed in PBS twice to remove the ethanol. Next, bone marrow-derived cells were acquired through α-MEM irrigation using a sterilized syringe. Afterward, the flushing fluid was collected under filtration using a cell sieve with a mesh size of 40 μm and further centrifuged at a speed of 1200 rpm for 5 min. After that, the supernatant liquor was removed, and the cellular entities were reconstituted and transferred to a 10-cm cell culture dish. The cells were cultivated in α-MEM medium enriched with 10% FBS and 1% (v/v) penicillin (100 U/ml)/streptomycin (100 μg/ml) and 292 mg/l L-glutamine and then incubated in an atmospherically moistened milieu with a 5% concentration of CO_2 at 37°C. The solution underwent renewal on a bi-daily basis and cell passages were performed once the cell density touched 70–80%. Cells in passages 3–5 were employed for the subsequent cellular experiments. MC3T3-E1 were resuscitated and cultured under the same conditions.

EGFP transfection efficiency and cell viability

Before detecting the gene delivery ability of DAM, the RLS transfection ability in MC3T3-E1 and BMSCs cells was detected at various nitrogen-to-phosphorus (N/P) ratios. Briefly, cells were evenly distributed in 96-well culture plates with a density of 1×10^4 per well. After a lapse of 24 h following cellular adhesion, the culture medium was substituted for the fresh one, and pDNA lipoplexes with diverse N/P ratios were added (10 μl, 200 ng pEGFP per well). PEI/pEGFP at an N/P ratio of 10 and Lipo 2000/pEGFP were administered to the cells as the experimental control. After 4 h of cultivation at 37°C, the medium was refreshed. Cells were raised for an extra 20 and 44 h and visualized using an inverted fluorescence microscope (IX73, Olympus). The mean fluorescence intensity (MFI) was determined by analyzing three samples with the assistance of ImageJ software. Followingly, the gene expression on various DAM-coated Ti was detected. The cells were seeded at 5×10^4/well into 24-well culture plates (Corning, USA) prepositioned with the discs of FG Ti, FG Ti-P/pEGFP-1, FG Ti-P/pEGFP-6 and CG Ti-P/pEGFP-6 for 24 h incubation. Likewise, the cells on Ti discs were visually examined and further analyzed. Furthermore, the cytocompatibility was investigated by CCK-8 assay by analyzing the cell viability of BMSCs transfected with the above-mentioned Ti samples for 24 h. All the above samples were incubated with 10% CCK-8 for another 1-h incubation and then measured by a microplate reader (Bio-Rad 550, USA) at 450 nm. Finally, the cell viability was calculated.

The spreading and migration of BMSCs cells on DAM deposited Ti

The cell cytoskeleton orientation on DAM-coated Ti was observed by rhodamine-phalloidin. First, the cells were evenly distributed onto various Ti samples at an intensity of 5×10^4/well for 36 h. Subsequently, the cells were immersed in 4% paraformaldehyde and fixed for 10 min, followed by permeabilization with 0.5% Triton X-100 for 5 min. To visualize the cytoskeleton, the staining lasted for 30 min using rhodamine phalloidin. Additionally, the nuclei were labeled with DAPI for 2–3 min, respectively. Finally, cells were washed and observed by confocal laser scanning microscopy (CLSM, LSM880, Zeiss). ImageJ was employed to calculate the spreading area, aspect ratio and attachment angle of the cell, and the RD along the FG Ti long axis was defined as 0°.

Cell migration on DAM-coated Ti substrates in real-time was monitored using a live cell imaging system (DMI6000B, Leica). As mentioned previously, BMSCs were sowed and cultured on various Ti substrates. After an incubation period of 36 h, the origin culture medium was eliminated, and then the live cell tracker CMFDA was added (0.5 μmol/l). After the labeling process lasted for 30 min in the dark environment at 37°C, cells were observed and then tracked for 12 h at 5-min intervals in real time. Cell movement trajectories were tracked using the in-built affiliated particle tracking module. Net displacement refers to the magnitude of the vector that directly connects the starting and ending points of the cell paths. The mean cell displacement during each time interval of a certain path was used to compute velocity. The entire distance of movements along the path was used as the definition of distance traveled. Origin 2021 software was used to determine and analyze cell migration trajectories.

Cellular uptake evaluation on different Ti substrates

BMSCs cells were first seeded onto naked FG Ti and CG Ti substrates at an intensity of 5×10^4/well for 24 h adhesion and spreading. After that, the cells were transfected with Cy5-labeled RLS/pGL3 lipoplexes at preferred N/P 30. After co-incubation for 2, 4 and 6 h, cells were fixed with a solution containing 4% paraformaldehyde for 10 min. Following this, they were permeabilized by immersing them in a 0.5% solution of Triton X-100 for 5 min. The cytoskeleton was labeled for 40 min employing FITC-phalloidin totally, while the nuclei were stained with DAPI for 2–3 min, correspondingly. After a thorough wash, the cellular uptake was verified quantitatively using distinct methodologies. The first approach involved semi-quantification was performed using the MFI parameter in ImageJ software. The second method employed a flow cytometer (FC, FC500, BD Biosciences), wherein the BMSCs cells were enzymatically digested from the Ti samples after a 6-h endocytosis period, centrifuged (3 min, 1200 rpm) and subsequently resuspended in 300 μl PBS for detection in the allophycocyanin channel.

pBMP2 expression of BMSCs by quantitative real-time polymerase chain reaction and western blot in vitro

The BMSCs cells were cultivated and sowed on various Ti discs. After 48 h incubation, the RNA from cells was extracted and subjected to reverse transcription. The quantification of the mRNA expression level of BMP2 was assessed through the utilization of a quantitative real-time polymerase chain reaction system (Q-PCR, CFX96™, Bio-Rad) in combination with the SYBR Green chimeric fluorescence method. The primer sequences corresponding to BMP2 are shown in Supplementary Table S1. The expression of GAPDH was chosen as the reference to normalize the expression level.

The protein expression levels of BMP2 in BMSCs were followingly detected by WB assay. Briefly, the treated cells were subjected to lyse using RIPA lysis buffer supplemented with a cocktail of protease inhibitors. Next, cells were solubilized and subsequently subjected to centrifugation at 12 000 rpm for 15 min at 4°C to obtain the supernatants. The quantification of protein concentrations in the supernatants was scrutinized via a BCA assay. An equal amount of protein among different experimental groups was sampled and separated on the gel for 2 h. After separation, the proteins were moved to a polyvinylidene

fluoride membrane (100 V, 40 min). Afterward, the membrane was obstructed in PBS with 5% non-fat milk to reduce background noise. Followingly, the membrane was incubated with recombinant rabbit anti-BMP2 (EPR20807, Abcam, UK), anti-β-actin antibodies (Beyotime, China) and goat anti-rabbit IgG-HRP antibody (Beyotime, China) sequentially. Finally, the color development reaction was conducted and the protein band was visualized with an imaging system (ChemiDocTM XRS$^+$, Bio-Rad).

In vitro osteogenesis and mineralization evaluation

BMSCs cells were seeded at 5×10^4/well into 24-well culture plates prepositioned with the discs of FG Ti, FG Ti-P/pBMP2-6 and CG Ti-P/pBMP2-6 for 3, 7 and 14 days. At scheduled time points, the cells on the Ti surface were harvested and subjected to the analysis of osteogenic differentiation by the Q-PCR system regarding the pBMP2 expression of BMSCs by quantitative real-time polymerase chain reaction and western blot *in vitro* section. The primers for the investigated osteogenesis-related genes including BMP2, osteopontin (OPN), osteocalcin (OCN), alkaline phosphatase (ALP), collagen type I (Col 1a), and runt-related transcription factor 2 (Runx2) were listed in Supplementary Table S1. The capacity of BMSCs to mineralize the matrix on DAM-modified Ti was assessed by employing the ARS coloring test. Briefly, after 7 days of cultivation, the cells grown on different Ti samples were rinsed thrice with PBS gently, followed by the fixation of 4% paraformaldehyde solution for 15 min. Next, the cells were washed thoroughly with PBS three times to remove any residual fixative and stained with 1% (w/v) ARS solution for 30 min. After washing thrice with deionized water, the stained cells on the Ti substrate were visualized under the lens of an inverted metallographic microscope (ECLIPSE MA100, Nikon) and quantitatively analyzed by ImageJ.

Antibacterial performance *in vitro*

Bacterial culture

Staphylococcus aureus (ATCC29213) and *E.coli* (ATCC8739) were employed as prototypical Gram-positive and Gram-negative bacteria, separately. Both bacteria were cultivated in Luria–Bertani medium (LB) and shaken continuously at 37°C (220 rpm).

Antimicrobial performance of DAM-coated Ti in vitro

The antibacterial activities of DAM components including P, RLS and a mixture of P and PLS (1/6, v/v) were initially appraised through the reduction in colony-forming units (CFU), succeeded by the utilization of the agarose plate technique. Detailly, 100 μl of the prepared microbial suspension in the logarithmic growth phase (1×10^6 CFU/ml) was taken and incubated with 400 μl of PBS (the control group) or equal volume lysozyme, P, RLS, a mixture of P and PLS (1:6, v/v) solution (the experimental group) for 1 h at 37°C. After incubation, the bacteria were serially diluted 10^4 times with PBS. A volume of 100 μl of these diluted bacteria was evenly spread onto solid agar plates. After incubation at 37°C for a duration of 18 h, the number of colonies was totaled by ImageJ, and the antibacterial rate was calculated. Likewise, the prepared bacteria suspension with the same concentration was seeded into a 24-well plate prepositioned with various Ti discs for 24 h at 37°C. All Ti samples with attached microorganisms were washed quartic with 5 ml sterilized PBS each time and the eluent was collected. Then, 15 μl of the eluent was uniformly coated on LB agar plates, and then these plates were incubated inverted for 18 h at 37°C. The number of colonies was counted by ImageJ. The quantification of CFU reduction was determined by employing the following equation:

$$\text{Antibacterial rate}(\%) = \frac{\text{CFU of the control group} - \text{CFU of the experimental group}}{\text{CFU of the control group}} \times 100 \quad (1)$$

The experiment group was referred to as the DAM-coated Ti/DAM solution group, and the control was considered as the blank Ti/PBS solution group.

The morphologies of adherent bacteria on various Ti discs were detected visually using FE-SEM. Briefly, 1 ml of bacterial dilution with a concentration of 1×10^6 CFU/ml was added to a 24-well plate prepositioned with various Ti samples for cultivation of 12 h at 37°C. After discarding the medium, all Ti discs were rinsed thrice thoroughly with PBS. The bacteria were then immobilized on Ti surfaces with glutaraldehyde (2.5 wt%) for 1 h. Followingly, Ti samples were sequentially dehydrated using progressively increasing concentrations of graded ethanol (30%, 50%, 70%, 80%, 90%, 95%, 100% and 100%, v/v) for 10 min each time. At last, they were desiccated under a vacuum and coated with a layer of gold for observation by FE-SEM. To observe the internal structure of bacteria after RLS (1 mg/ml) treatment, they were centrifuged to collect, prefixed with glutaraldehyde (3.0 wt%), then the tissue was fixed through a series of processes including postfixed, dehydrated, infiltrated, embedded and stained. The structural characteristics of stained sections were thoroughly examined using a transmission electron microscope (TEM, JEM-1400-FLASH, JEOL).

Animals and surgical procedures

Surgical procedure

Before DAM coating, all Ti rods (FG Ti) were ultrasonically cleaned and sterilized as described previously. Specific pathogen-free female 8-week-old SD rats (weighing 200–300 g) were chosen in this research. All animal experiments performed in this study were carried out under the approval of the Ethics Committee of Huaxi Animal Experiments at Sichuan University, with the assigned Ethics Record number 20211196A. Every possible effort was made to minimize any potential suffering experienced by animals and to minimize the overall number of animals utilized in the study. All rats were randomly divided into three groups for FG Ti, FG Ti-P/pEGFP-6 and FG Ti-P/pBMP2-6 implant placement. Each group comprised 10 rats, half of which were assigned to the third-week group, and the other half to the sixth-week group. Rats were administered anesthesia utilizing 2% pentobarbital sodium to ensure their comfort via intraperitoneal injection at a dose of 30 mg/kg. The right and left hind limbs were carefully shaved and the knee joint was positioned and secured in maximum extension. To unveil the lateral femoral condyle, a precise decision measuring merely 8 mm was made along the longitudinal axis, positioned near the patellar ligament. A cylindrical bone defect (diameter: 2 mm, depth: 4 mm) was created by drilling using a 2-mm diameter drill bit and washed with saline to remove debris and cool the bone. A cylindrical Ti implant per leg was inserted into the bone defects. The surgical site was irrigated with saline to ensure cleanliness and the opening was meticulously sutured at every layer. To alleviate postoperative discomfort, all rats were administered buprenorphine (Temgesic, Reckitt & Cloman, Hull, UK) injections for 3 days following the surgical procedure. Simultaneously, enrofloxacin was administrated intramuscularly at a dose of 10 mg/kg to mitigate the potentiality of postoperative infection. The rats were euthanized in the third and sixth weeks to collect the femur, respectively. The sixth-week experimental group was continuously fluorescently labeled

and intraperitoneally injected with CA at a dosage of 30 mg/kg, and TE at a dosage of 30 mg/kg at 14 and 3 days before the euthanasia, respectively.

Micro-computed tomography analysis

For micro-computed tomography analysis (micro-CT, Quantum GX II, Perkin Elmer) analysis, specimens of femoral condyles with implants were procured and immersed in a 4% paraformaldehyde solution for a minimum duration of 24 h to ensure proper fixation. After the removal of excessive bone tissue from the distal femur, the femoral condyle of each group with implants underwent scanning via a micro-CT system. The scanning was performed at a resolution of 18 μm, utilizing a voltage of 90 kV and a current of 80 μA. Three-dimensional (3D) reconstruction was performed by Mimics Medical 21.0 software. The region around the implant with a diameter of 1 mm was considered the region of interest. A threshold range spanning from 270 to 5000 was applied to discern newborn bone at the juncture of the bone/implant interface in contrast to Ti. After implementing the reconstruction, various quantitative parameters were used to assess osseointegration surrounding the implant. These parameters included bone volume (BV), bone volume fraction (BV/TV), bone mineral content (BMC), bone mineral density (BMD), trabecular numbers (Tb. N), trabecular separation (Tb. Sp) and trabecular thickness (Tb. Th) of the defect area.

In vivo histological examination

After implantation for 6 weeks, the femoral condyles collected from rats were first immersed in 4% paraformaldehyde for fixation, and then hard tissue sections in the sixth week were prepared by a diamond tissue saw slicing (SAT-001, Aorigin). Subsequently, the sections were colored with a solution of 1% toluidine blue for 1 min and observed histologically via an advanced pathology imaging system (Vectra 3, PerkinElmer). Quantitative analysis of the area of the newly formed bone and the length of new bone tissue around the implant (mm) was performed by Image-Pro-Plus. The bone–implant contact (BIC) rate was calculated as follows:

$$\mathrm{BIC}(\%) = \frac{\text{Length of new bone tissue around the implant (mm)}}{\text{Peri–implant length (mm)}} \times 100 \quad (2)$$

Moreover, the fluorescence emitted by CA (with an excitation wavelength of 488 nm) and TE (with an excitation wavelength of 405 nm) was examined by the CLSM. The inter-labeled width between CA and TE fluorescence (mm) was counted by Image-Pro-Plus. The bone mineral apposition rate (MAR) was determined by the subsequent equation:

$$\mathrm{MAR}(\%) = \frac{\text{Average distance between double bars of fluorescence (mm)}}{\text{Fluorescent labeling intervals (d)}} \times 100 \quad (3)$$

Statistical analysis

All data were represented as the average ± standard deviation (SD). A one-way analysis of variance (ANOVA) was employed to ascertain statistical significance, followed by Tukey's *post hoc* test for further analysis. A significance level of $P < 0.05$ was used to determine the statistical significance. GraphPad Prism was employed to perform the statistical analysis.

Results and discussion

Fabrication and surface characterization of plasmid DNA-activated matrix-coated Ti samples

To boost the efficient osteointegration of Ti implants, protein coatings, especially for BMP2 protein have been extensively utilized in orthopedic surgery. However, its rapid elimination from the body and susceptibility to deactivation require higher-than-normal doses, which may result in neurological, acute respiratory and inflammatory issues. To achieve long-term functionality and stability, DAM was introduced onto the Ti surface by LBL self-assembly technology as an alternative to protein coatings. The Ti interface was firstly modified with phase transition lysozyme (P) which not only stably adhered to the surface through amyloid nanostructures but also imparted positive charges, allowing for further functionalization [34]. Moreover, P exhibits a wide range of antibacterial properties and possesses high biocompatibility, making it a promising candidate for implant applications [28, 34]. As visualized by FE-SEM, a uniform and thinner film-like coating of P was formed on the Ti substrate.

Next, the negatively charged pDNA (a BMP2-expressed plasmid) was electrostatically anchored, achieved by the interaction with the positive charges onto the surface of P-coated Ti, followed by the positively charged arginine-rich lipids anchoring (RLS, Supplementary Figure S1), resulting in the formation of multiple layers of pDNA and RLS (n is the numbers of bilayers), denoted as (pDNA/RLS)n (Figure 1A). As the number of bilayers grew, pDNA/RLS nanocomposites progressively fused into larger clusters and aggregates as noted in published reports [35] (Figure 1B and Supplementary Figure S3A). Six bilayers of DAM films largely retained the fibrous topology of FG Ti while seven bilayers almost completely masked all the specific structures. As a result, $(\mathrm{pDNA/RLS})_6$ were chosen for the following evaluations. Of note, the different substrates had minimal impact on the morphology of DAM film assembly, with similar patterns observed on FG Ti, CG Ti and smooth silicon wafers.

Similar to FE-SEM results, the roughness of different samples couldn't be affected by different substrates in the AFM test, but rather determined by the number of bilayers in the DAM films. Specifically, $(\mathrm{pDNA/RLS})_6$ film showed approximately a ~3-fold increase in roughness compared to uncoated and one bilayer film (Figure 1C and D and Supplementary Figure S3B). This shift in roughness could be explained by coiled conformations of deposited molecules, which result from the enhanced intermolecular interactions by increased layers [35]. Meanwhile, the $(\mathrm{pDNA/RLS})_6$ provided a dramatically decreased Young's modulus (338.0 MPa) compared to uncoated FG Ti (2984.8 MPa), approaching the mechanical property of natural bones (~15 MPa) [36], indicating a reduced stress shielding of metal implants. Besides, Young's modulus of $(\mathrm{pDNA/RLS})_6$ was much higher than that of P coating (~106-fold) and one bilayer (~4.5-fold), probably due to the higher ionic strength of RLS (Figure 1E) [37]. Water contact angle measurements were then conducted to investigate the hydrophilic behavior of different Ti samples (Figure 1F). The DAM deposition made the surface more hydrophobic probably because of the exposure of hydrophobic residues in RLS located at the outermost layer [37, 38]. Moreover, one bilayer of DAM film retained the difference in wettability between 0° and 90° along the RD of FG Ti from the anatase TiO_2 (102)-dominated surfaces [26]. However, the difference diminished as the film thickness increased to six layers.

During the process of DAM assembly on PLA sheets, there were fluctuations in surface zeta (ζ) potential (Supplementary

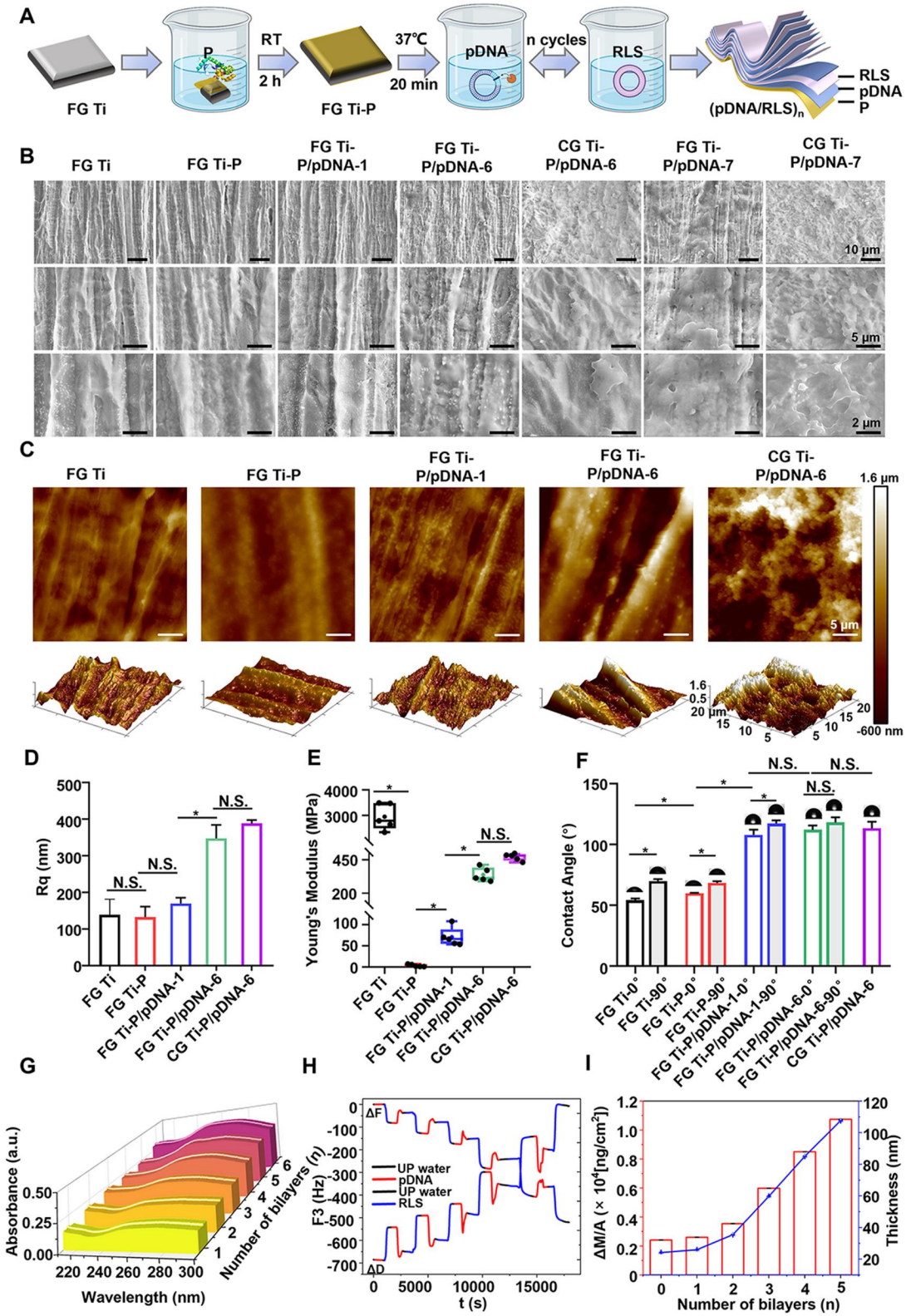

Figure 1. Fabrication and characterization of the DAM composed of multilayered film $(pDNA/RLS)_6$ on different Ti samples. (**A**) Illustration of the preparation process for DAM on Ti substrates. P was first deposited on the Ti, followed by sequential and repeated adsorption of pDNA and RLS *n* cycles to obtain the multilayer film $(pDNA/RLS)_n$. (**B**) FE-SEM images of the surface morphology of various Ti samples. (**C**) 2D and 3D AFM images of different Ti samples (20 μm × 20 μm). (**D**) Root mean square roughness (Rq) of the different substrates obtained by AFM. (**E**) Young's modulus of DAM films was obtained by AFM imaging of indentations and calculated by the Herz sphere model. The film was built up on the same specimen and five random spots were scanned. (**F**) The water contact angle degree (°) and image of different Ti samples. (**G**) Detection of the pDNA adsorption as a function of bilayer number during the multi-layer DAM fabrication by the solid UV-vis using the diffuse reflection module. (**H**) The real-time shifts of frequency (Δ*F*) and dissipation (Δ*D*) and (**I**) mass change per unit area (Δ*M*, μg/cm^2) and corresponding thickness (nm) during the multi-layer fabrication, which were monitored by the QCM-D sensor. *$P < 0.05$, NS, no significance.

Figure S4). The surface ζ potential increased by 35.1 mV due to the deposition of positively charged P on the PLA (a substitute for Ti) surface. After incubating with negatively charged pDNA, ζ potential showed a decrease of 37.2 mV. However, when positively charged RLS was immobilized on the surface, it rose again by 37.7 mV. These specific ζ potential fluctuations were continuously monitored in every cycle of multilayer film preparation, indicating successful layer-by-layer assembly of DAM films based on electrostatic interaction force. Moreover, the XPS spectra of several Ti samples also confirmed that P, pDNA and RLS had been effectively incorporated into DAM nanofilms (Supplementary Figure S5 and Table S2). Furthermore, the involvement of the DAM core component, pDNA, was evaluated by solid UV-vis. The results showed that pDNA adsorption increased linearly with an increasing number of bilayers (Figure 1G and Supplementary Figure S6).

The real-time quantification of $(pDNA/RLS)_6$ thin film assembly was further studied using a QCM-D (Figure 1H) and ellipsometry (Supplementary Figure S8). As the adsorption time increased, the frequency shift (ΔF) linearly decreased while the dissipation (ΔD) increased symmetrically, indicating the successive deposition of films on the substrate with flexible properties [39]. Moreover, RLS exhibited a greater ΔF than pDNA, probably because of its higher polymer concentrations [38, 40] (Figure 1H). Additionally, the total wet amount of absorbed $(pDNA/RLS)_6$ film was 10 737.7 ng/cm^2 with a pDNA loading amount of 2646.8 ng/cm^2 [41] (Figure 1I and Supplementary Figure S7). The result was significantly higher than reported for LBL films [8], probably due to the formation of a more powerful double-dentate hydrogen bond between the guanidine group in RLS and the phosphate group in pDNA. The thickness of $(pDNA/RLS)_6$ film was 107.6 nm by QCM-D (Figure 1I) and 163.7 nm by ellipsometry (Supplementary Figure S8).

Under physiological conditions, coating stability is essential for long-term functionality and safety. Thus, we evaluated the stability of DAM films through pDNA release (Supplementary Figure S9). The remaining pDNA amount loaded (97.9%) on the specimen did not significantly differ along with incubation time, indicating long-lasting stability, which may be attributed to the strong adherence of P [34] and the double-dentate hydrogen bond between RLS and pDNA.

The high pDNA transfection and viability on DAM-coated Ti surface

pEGFP transfection was then employed to evaluate whether the DAM coating combined fibrous FG Ti substrate could promote pDNA transfection efficiency, which has been a major challenge in DAM-based tissue repair [42]. As shown in Figure 2A, the DAM coating successfully delivered pEGFP into both BMSCs and MC3T3-E1 cells, which could differentiate into osteoblast cells under certain conditions. Furthermore, six layers of pDNA/RLS film showed a 1.4–3.0-fold increase in transfection efficiency compared to one layer on FG Ti. Statistically, FG Ti-P/pEGFP-6 achieved the highest expression with 75.7% in BMSCs (Figure 2B and Supplementary Figure S11). Notably, the FG Ti-P/pEGFP-6 demonstrated significant advantages over CG Ti-P/pEGFP-6, exhibiting a 3-fold higher fluorescence intensity in BMSCs and a 1.4-fold increase in MC3T3-E1. These findings suggested that the fibrous structure on FG Ti may positively influence gene transfection. It has been reported that micropatterns can manipulate cell adhesion, spreading, elongation and migration by remodeling the cytoskeleton [20, 43]. The polymerization of the F-actin network is also potentially involved in endocytosis processes, including the invagination, contraction, division and movement of vesicles [44]. Followingly, the cytotoxicity of various Ti samples was evaluated and all groups showed good compatibility with over 90% of cells surviving after exposures. We speculated that the low toxicity might be attributed to the intracellular degradation of disulfide linkage in RLS [29, 30] and the good biocompatibility of P [34] (Supplementary Figure S12).

Thus, we initially confirmed if six bilayers of pDNA/RLS film would affect the oriented cytoskeleton alignment induced by fibrous FG Ti, as reported previously [26]. As shown in Figure 2C and D and Supplementary Figure S13, no significant difference in cell orientation was observed before and after $(pDNA/RLS)_6$ film coating on FG Ti, with $\geq$ 90% cell spreading ($-15° < \theta < 15°$ along the RD) as reported previously [24]. Interestingly, the cell spreading aspect ratio and area even showed an obvious increase after DAM modification due to the polyelectrolyte multilayers providing a more compatible interface for cell adhesion. In contrast, cells on CG Ti-P/pGL3-6 were randomly distributed. Besides, the corresponding cell movement behavior on DAM-coated Ti was monitored (Figure 2E and F and Supplementary Figure S14), as it is largely influenced by the cytoskeleton. On the naked and DAM-modified FG Ti, cells tended to migrate parallel to the fibrous grain. Statistically, FG Ti-P/pGL3-6 achieved the highest cell migration velocity and net displacement compared to naked FG-Ti and CG Ti-P/pGL3-6, indicating prominent bone healing. Moreover, the strengthened migration ability may also contribute to enhanced gene transfection. It's probable that cell migration is dependent on integrins, which are known to trigger cytoskeleton rearrangement, thus affecting endocytosis and nuclear translocation of DNA [45–48].

Next, we investigated whether the oriented cytoskeleton could enhance the cellular uptake of pDNA lipoplexes (Figure 2G and H and Supplementary Figure S15). After co-incubation with Cy5-labeled RLS/pGL3, the cells seeded on FG Ti showed significantly stronger red fluorescence compared to those on CG Ti. Specifically, the mean fluorescence intensity increased by 34.5%, 44.4%and 59.8% at 2, 4, 6 h, respectively (Supplementary Figure S15). This difference was further confirmed by quantitative flow cytometer analysis, which revealed a higher percentage of Cy5-positive cells in the FG Ti group (84.4%) compared to the CG Ti group (68.5%) (Figure 2H).

Besides, we compared the gene delivery efficiency of RLS with that of Lipo 2000 and PEI in BMSCs and MC3T3-E1 cells (Supplementary Figure S10). The results confirmed the superiority of RLS as a gene vector. That is to say, the high gene delivery efficiency observed in BMSCs and MC3T3-E1 cells with FG Ti-P/pDNA-6 may originate from a high loading amount of pDNA in multilayered films, outstanding delivery efficiency of RLS vector and surface fibrous topology on FG Ti.

Improved osteogenesis on DAM-coated Ti surface *in vitro*

Encouraged by the efficient gene delivery of the DAM system coated on the Ti surface, the expression of therapeutic pBMP2 at mRNA and protein levels was evaluated (Figure 3A). In the Q-PCR analysis, Again, FG Ti-P/pBMP2-6 exhibited significantly higher mRNA expression levels than that of FG Ti (9.7-fold), FG Ti-P/pBMP2-1(1.7-fold) and CG Ti-P/pBMP2-6 (1.2-fold). The WB results further confirmed that the pBMP2 was successfully translated into protein, with a 1.6-fold increase than that of un-transfected BMSCs (Figure 3B and C). Besides, the efficacy of constructed BMP2 plasmid was further verified by detecting the expression of downstream osteogenic-related genes. As shown in

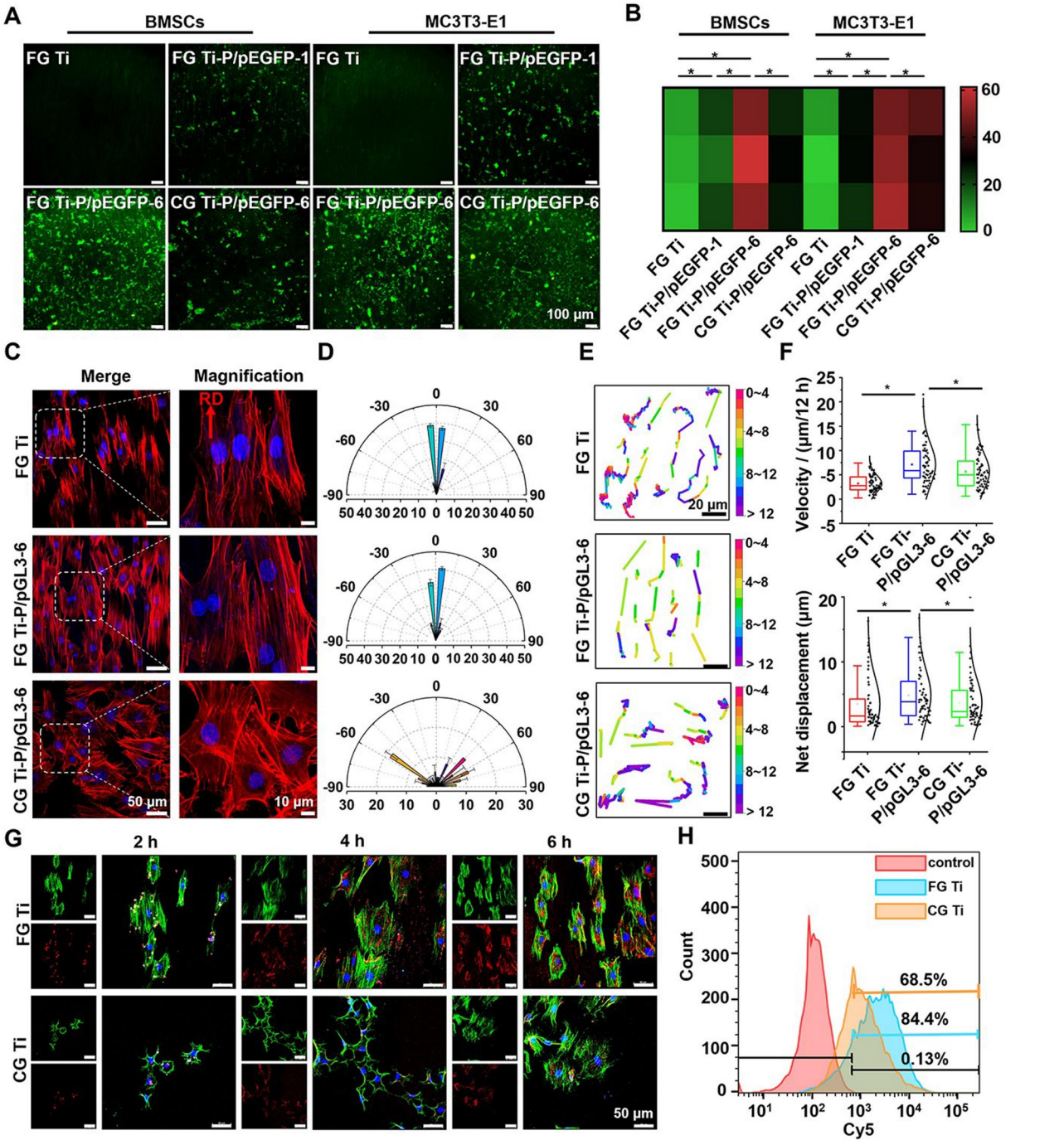

Figure 2. Transfection efficiency and contact guidance phenomenon of DAM on different Ti samples. (**A**) Fluorescence microscopy pictures and (**B**) MFI analysis of BMSCs and MC3T3-E1 cells transfected with pEGFP on different Ti samples. Scale bar: 100 μm. (**C**) Representative morphology of BMSCs observed by CLSM with phalloidine stained cytoskeleton protein F-actin (red) and DAPI stained nucleus (blue) after 36 h-culture on different Ti substrates. Scale bars: 50 or 10 μm. White dotted box: magnification areas. (**D**) Cell-orientation analysis on different Ti samples, calculated by the cell occurrence frequency (%) and angles (°) along the rolling direction (RD) of FG Ti and arbitrary direction of CG Ti. (**E**) Analysis of the BMSCs movement. The migration trajectory of BMSCs on different Ti surfaces was monitored by a live cell imaging system. The cells were imaged at 5-min intervals for 12 h. (**F**) Scatterplot and box plot of cell migration velocity and net displacements, together with the normal curve ($n = 50$). In the box plots, the median is represented by the middle line, while the top and bottom of the box correspond to the 75th and 25th percentiles, respectively. The whiskers extend to the 90th and 10th percentiles, providing an overview of the data's spread. (**G**) CLSM observation of uptake of Cy5-labeled RLS/pGL3 lipoplexes by BMSCs on CG Ti and FG Ti substrates after 2–6 h incubation. Red: Cy5-labeled RLS/pGL3 lipoplexes, green: FITC-phalloidin-labeled F-actin, blue: DAPI-labeled nucleus. Scale bar: 50 μm. (H) Internalized Cy5-labeled RLS/pGL3 complexes of BMSCs on CG Ti and FG Ti substrates after 6 h incubation, detected by flow cytometry. *$P < 0.05$, NS, no significance.

Supplementary Figure S16, pBMP2 induced obvious upregulation of most osteogenic genes compared to pEGFP transfection after 7 days of differentiation.

Followingly, the osteogenic differentiation of BMSCs on the pBMP2 incorporated DAM-coated Ti surface was detected, by calcium nodule staining after 7 days of incubation (Figure 3D).

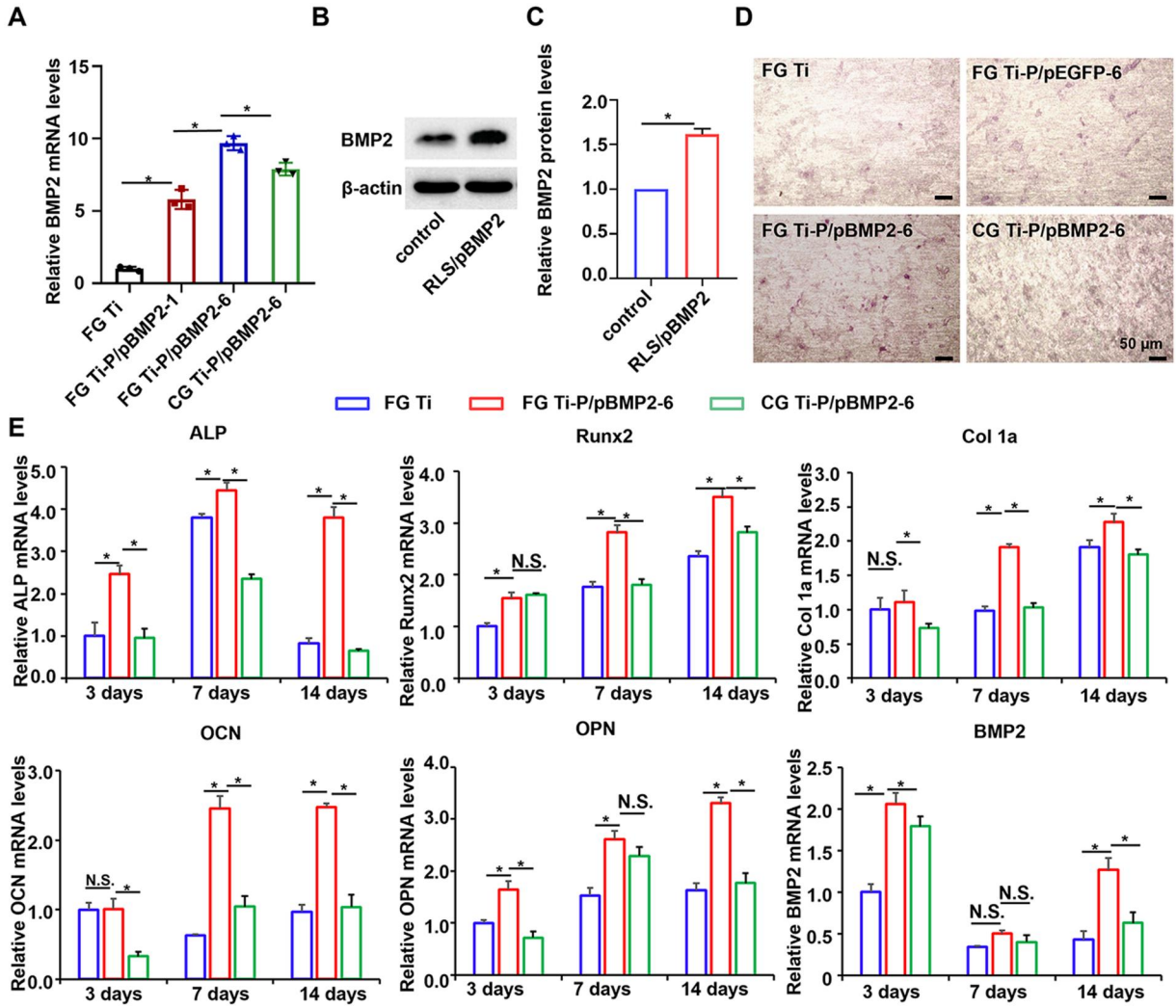

Figure 3. The osteogenic capacity of BMSCs on different Ti samples *in vitro*. (**A**) Q-PCR analysis of BMP2 mRNA levels in BMSCs cells cultured on different Ti substrates for 48 h. (**B**) WB band and (**C**) related semi-quantitative analysis of BMP2 protein levels in BMSCs cells transfected with RLS/pBMP2 lipoplexes at a preferred N/P ratio of 30 for 48 h. β-actin was considered as a housekeeping control. (**D**) ARS staining of BMSCs cultured on the different Ti surfaces for 7 days. Scale bar, 50 μm. (**E**) the relative mRNA expression of the osteogenic marker gene in BMSCs cultured on the different DAM-deposited Ti samples for 3, 7 and 14 days. All values were standardized according to the expression of GAPDH. *$P < 0.05$, NS, no significance.

Briefly, FG Ti-P/pBMP2-6 and CG Ti-P/pBMP2-6 enabled evident calcium nodules generation compared to FG Ti, showing 2.5-fold and 1.7-fold increases, respectively, indicating that the advantage of pBMP2 modified DAM in promoting mineralization. Moreover, more calcium nodules were formed on FG Ti-P/pBMP2-6 compared to CG Ti-P/pBMP2-6, indicating the positive role of the fibrous topological structure of FG Ti during osteogenesis. In addition, there was a 1.7-fold coloring observed on the FG Ti-P/pEGFP-6 compared to FG Ti (Supplementary Figure S17). We hypothesized that the transitional DAM film positively contributed to stem cell osteogenesis even without the therapeutic genes.

Next, the marker genes related to osteogenesis differentiation were detected by Q-PCR analysis in BMSCs cultured on pBMP2 incorporated DAM-coated Ti surface for 3, 7 and 14 days (Figure 3E). ALP is an important marker during early osteogenic differentiation [49], of which peak expressions generally appeared at 7 days. BMSCs cultured on FG Ti-P/pBMP2-6 showed a 1.3 and 1.9-fold enhanced expression of ALP compared to CG Ti-P/pBMP2-6 and uncoated FG Ti, respectively. After 14 days of culturing, the difference remained although these genes were downregulated as differentiation progressed. The expression levels of Runx2, Col 1a, OCN and OPN genes, which served as marker genes for mid-to-late-stage osteogenesis [50, 51], exhibited an upward trend with culture time. The peak expression levels were observed at 14 days, demonstrating 1.5-fold, 1.2-fold, 2.6-fold and 2.1-fold expression increases on the FG Ti-P/pBMP2-6 surface compared to FG Ti, respectively. Besides, FG Ti-P/pBMP2-6 also induced more Runx2, Col la, OCN and OPN expression than CG Ti-P/pBMP2-6. That is to say, the DAM facilitated osteogenesis by enhancing BMP2 expression and specifical fibrous topology. Similarly, the FG Ti-P/pBMP2-6 group showed the greatest upregulation of mRNA levels of BMP2 at day 3, which showed a 2-fold and 1.2-fold enhanced expression compared to FG Ti, CG Ti-P/pBMP2-6, respectively. Notably, this difference disappeared after 7 days of induction, which was attributed to the gradual depletion of exogenous genes. After 14 days of culture, the BMP2 expression displayed an obvious augmentation in the FG

Ti-P/pBMP2-6 group potentially attributed to the promoted osteogenic differentiation.

Antimicrobial performance of the DAM-coated Ti surface *in vitro*

Abundant studies showed that bacterial infection is one of the primary factors preventing rapid bone integration [52, 53]. Once bacterial adhesion occurs on the implant surface, bacterial colonies and biofilms will gradually form and disrupt the function of the implant. RLS is rich in positive charge [54] and arginine [55, 56], which are believed to prevent early adhesion and disrupt membranes, leading to antibacterial performance. Additionally, P kills bacteria by interfering with the bacterial membrane [28]. Initially, the antimicrobial properties against *E.coli* and *S.aureus* on DAM-coated Ti were verified by the agarose plate assay (Figure 4A–C). Compared with FG Ti, there were much fewer *E.coli*

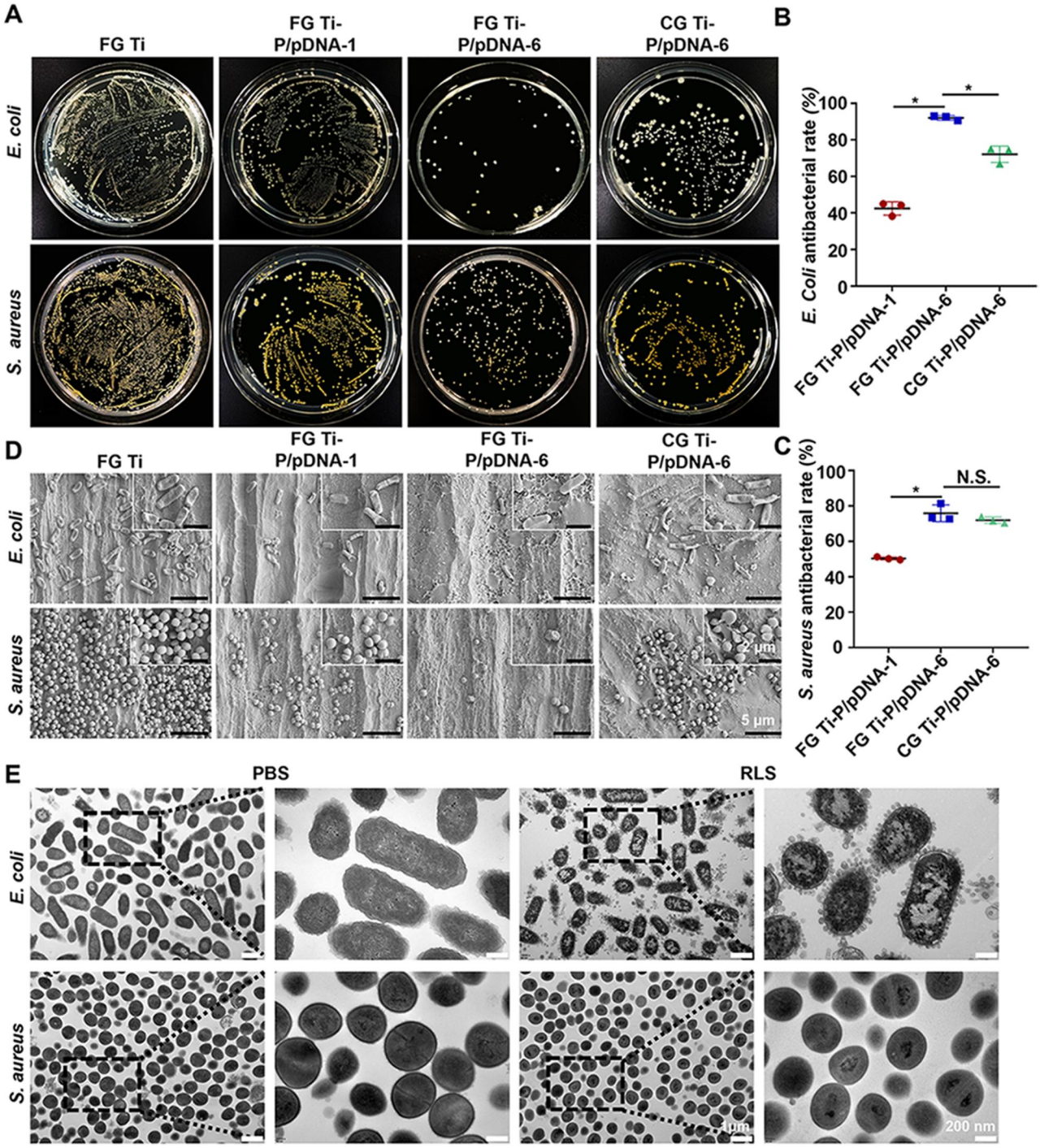

Figure 4. Antimicrobial evaluation of different Ti substrates *in vitro*. (**A**) *E.coli* and *S.aureus* colony formation on LB agarose plates for 18 h after culturing with different Ti substrates for 12 h. Antibacterial rates of (**B**) *E.coli* and (**C**) *S.aureus* were calculated by colony numbers normalized to the control group of FG Ti, $n = 3$. (**D**) FE-SEM observation of the early morphology of *S.aureus* and *E.coli* adhered on different Ti substrates for 24 h. White boxed regions were enlarged at the upper right corner. Scale bars: 5 or 2 μm. (**E**) TEM images of bacterial sections after being treated with PBS and RLS solution (1 mg/ml) for 1 h. Black dotted box: the magnification area. Scale bars: 1 μm, 200 nm. *$P < 0.05$, NS, no significance.

and *S.aureus* colonies on FG Ti-P/pDNA-1, FG Ti-P/pDNA-6 and CG Ti-P/pDNA-6. The statistical analysis revealed antimicrobial adhesion rates of 42.6% against *E.coli* and 50.4% against *S.aureus* for FG Ti-P/pDNA-1. In contrast, with the increasing amounts of RLS loaded on the DAM film, FG Ti-P/pDNA-6 could achieve a bacterial inhibition rate of 90% against *E.coli* and 80% against *S. aureus*. The antimicrobial efficacy of FG Ti-P/pDNA-6 can be attributed to the incorporation of RLS and P components. These additions individually achieved favorable resistance effects against bacteria, displaying inhibition rates over 96% against both *E.coli* and *S.aureus* (Supplementary Figure S18).

Afterward, *S.aureus* and *E.coli* adherents were counted, morphologically characterized, and analyzed for their antibacterial properties on the different Ti substrates. As portrayed in Figure 4D, in the FG Ti-P/pDNA-6 group, the adherent bacteria decreased along with bacterial membrane rupture and the exudation of bacterial contents. In contrast, the naked Ti surface exhibited substantial bacterial adhesion, with intact and smooth bacterial cell membranes. These findings may be due to the hydrophobicity of the surface preventing bacterial adhesion at the early stage of implantation. Followingly, as bacteria colonized the surface, the positively charged RLS and P molecules interacted with the phospholipid head groups in the bacterial membrane, resulting in membrane deformation and creating a favorable microenvironment for host cell adherence.

TEM images of bacterial ultrastructure revealed that treatment with RLS led to the formation of blebs and a significant decrease in intracellular content in most *E.coli* compared to the intact and smooth bacteria in the control group, indicating the disruption of bacterial walls [57, 58] (Figure 4E). In the case of *S.aureus*, condensation and precipitation of bacterial cytoplasmic contents were observed after RLS treatment, likely due to the difference in the outer envelope structure between Gram-positive and Gram-negative bacteria [59].

Fast osteointegration of DAM-modified Ti implantation

The new bone regeneration around the DAM-coated implants *in vivo* was evaluated using micro-CT scan reconstruction and analysis in the third and sixth weeks after implantation (Figure 5 and Supplementary Figure S19). The reconstructed 3D images showed the pBMP2-coated FG Ti yielded the highest new bone formation, with bone trabeculae closely aligned and covered around the implants in the third week (Figure 5A). These findings demonstrated a significant increase of 24.5% in BV, 22.7% in BV/TV, 49.7% in BMC and 50% in Tb. N, 42.5% in Tb. Th compared to

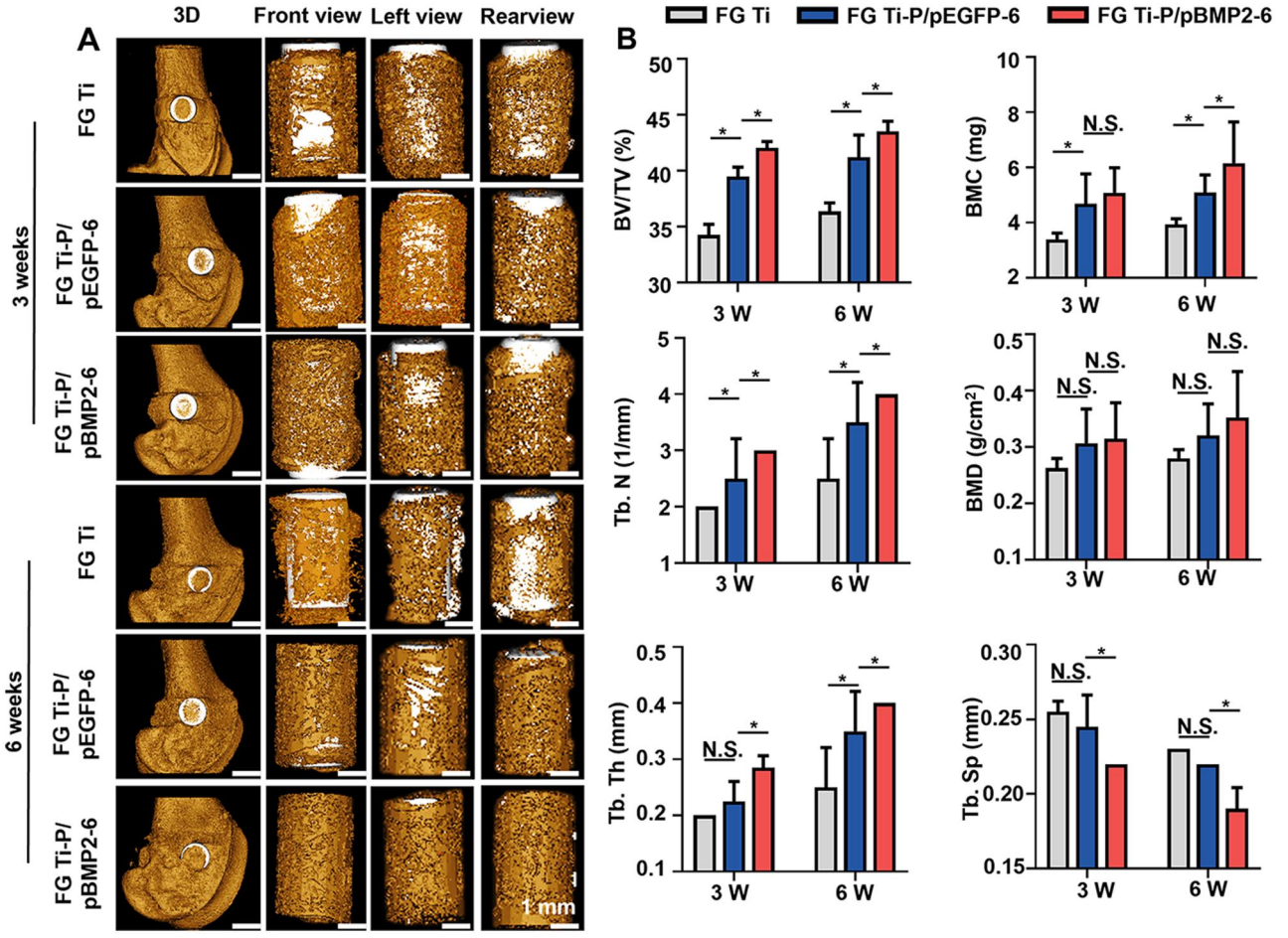

Figure 5. Osseointegration of FG Ti, FG Ti-P/pEGFP-6, FG Ti-P/pBMP2-6 rods at the third and sixth weeks after implantation. The implants were screwed into rods with a diameter of 2.0 mm, and length of 4.0 mm and placed at the rat femoral condyle. (**A**) 3D micro-CT reconstruction images of femoral condyles captured from various angles (front view, left view, rearview), showing the status of the implants and osteointegration progress after surgery at indicated time points. The acquisitions were performed on a micro-CT system at a resolution of 18 μm at 90 kV, 80 μA. (**B**) Micro-CT quantitative analyses of the osteogenesis indices, including BV/TV, BMC, BMD, Tb. N, Tb. Th, Tb. Sp in the third and sixth weeks using Mimics Medical 21.0 software within 1 mm around the implants ($n = 5$). pEGFP is a control for the osteogenic gene pBMP2. *$P < 0.05$, NS, no significance.

the control group of naked FG Ti. Besides, there was a notable reduction of 13.7% in Tb. Sp compared to the control group with sparsely arranged bone trabeculae. Additionally, FG Ti-P/pEGFP-6 also formed more dense bone trabeculae than the uncoated FG Ti group, with increases of 17% (BV), 15.3% (BV/TV), 15.3% (BMC), 25% (Tb. N), 12.5% (Tb. Th) and a decrease of 3.9% (Tb. Sp). Whereas BMD values were similar across the examined groups. After 6 weeks of implantation, a substantial increase in the formation of the new bone surrounding the implants was observed in all groups. The corresponding micro-CT analysis of BV, BV/TV, BMC, Tb. N, Tb. Th, Tb. Sp further confirmed the superior bone integration of FG Ti coated with pBMP2 compared to the naked Ti. Remarkably, even six bilayers of DAM films containing pEGFP exhibited accelerated progression of tissue regeneration, elucidating the potential of DAM to reduce stress-shielding effects without a therapeutic gene (Figure 5B). In a word, the FG Ti-P/pBMP2-6 implant achieved the most rapid osseointegration as a result of the synergistic action from the fibrous topography and the soft DAM films. Meanwhile, osteointegration was also observed by bone histomorphology in the sixth week of implantation (Figure 6). Firstly, the toluidine blue staining revealed extensive blue-colored areas around the FG Ti-P/pBMP2-6 implants, demonstrating the best bone continuity (2.3-fold vs. FG Ti), followed by FG Ti-P/pEGFP-6 (1.6-fold vs. FG Ti). In contrast, FG Ti displayed thin and sporadic sparse new bone growth (Figure 6A, C and D). Besides, the BIC of FG Ti-P/pBMP2-6 (94.3%) and FG Ti-P/pEGFP-6 (72.1%) were higher than FG Ti (47.3%). Furthermore, fluorescent labeling with CA and TE indicated the dynamic new bone formation and mineralization postoperatively (Figure 6B and E). The fluorescent labeling gap between the CA and TE exhibited a more substantial extension in both FG Ti-P/pBMP2-6 groups (a 5.8-fold increase) and FG Ti-P/pEGFP-6 (a 2.8-fold increase) compared to the FG Ti group, implying an accelerated osteogenesis caused by fibrous topology and the transitional DAM film.

Conclusion

In conclusion, we report a promising surface-mediated gene therapy strategy to solve the problem of surface biological activity of Ti implants combining the biocompatible DAM and favorable fibrous topology of the substrate. Through this approach, we significantly improved gene delivery efficiency, achieving a 30-fold increase compared to commercial PEI and Lipo 2000. This

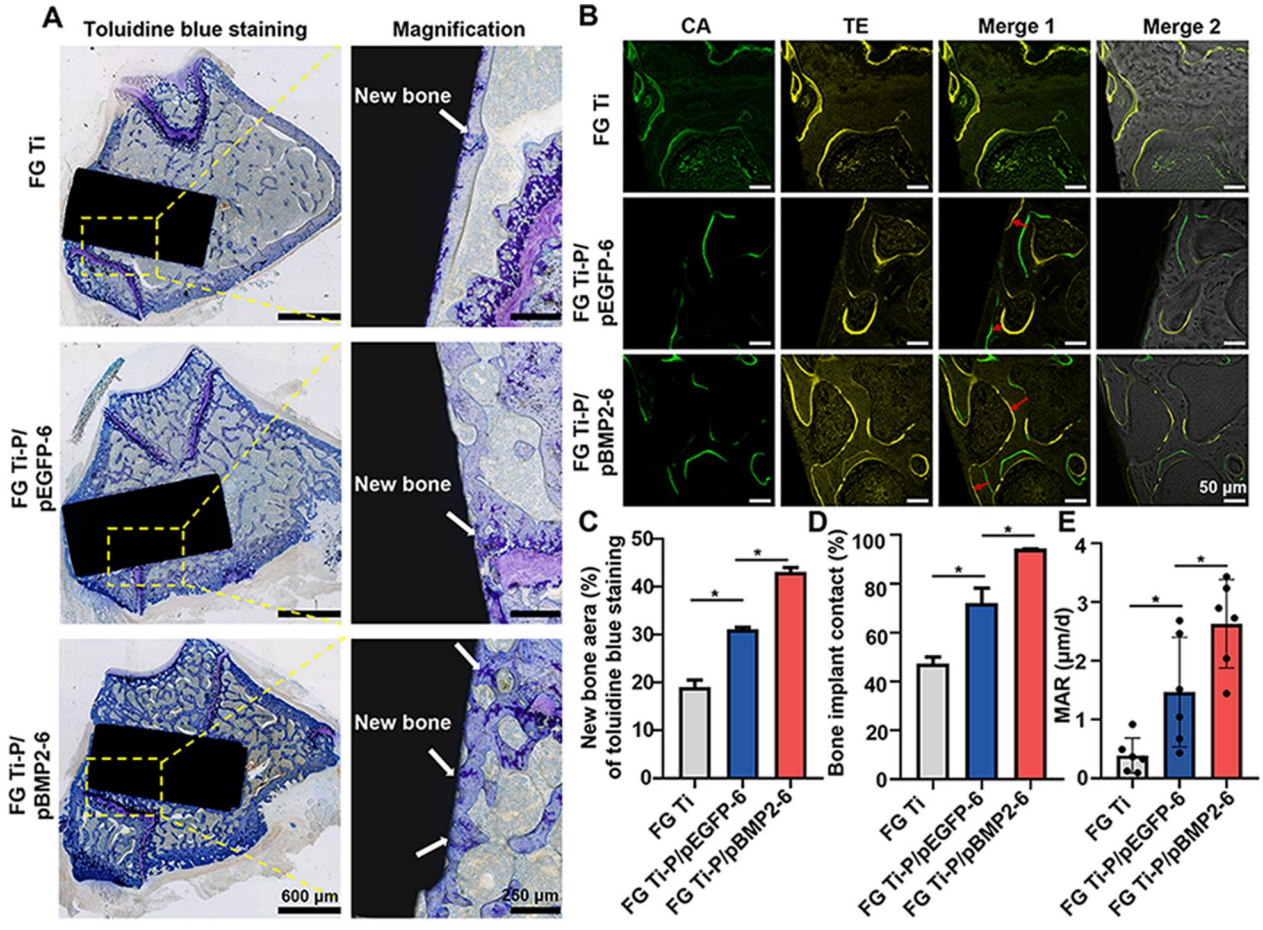

Figure 6. Bone integration effect of different Ti implants in the sixth week after surgery. (**A**) Optical microscope images of bone tissue around the different implants stained with toluidine blue on hard-tissue slices. Yellow dotted box: magnification areas. White arrows: new bone. Scale bars: 600 μm, 250 μm. (**B**) CLSM images of the new bone formation tissue around the implants of FG Ti, FG Ti-P/pEGFP-6 and FG Ti-P/pBMP2-6 by CA and TE labeling. The rats were serially intraperitoneally injected with CA (1%, w/w, 30 mg/kg) and TE (1%, w/w, 30 mg/kg) for 14 and 3 days before execution, respectively. The tissue sections were observed by CLSM with 488 nm (CA) and 405 nm (TE) excitation, respectively. Scale bar: 50 μm. The red arrows referred to the spacing between green and yellow fluorescence. Quantitative statistics of (**C**) new bone areas and (**D**) BIC by toluidine blue staining and (**E**) bone mineralization deposition rates (MAR) from CA and TE fluorescence labeling. $n = 5$, $^*P < 0.05$.

improvement is attributed to the high loading and activation of sufficient plasmid DNA (pDNA) using an efficient RLS vector, facilitated by the newly fabricated DAM system. Moreover, the efficacy was further enhanced by the surface fibrous topology. Upon exploration, the aligned micropattern can promote cellular uptake of pDNA and cell migration through remodeling the cytoskeleton. As a result of this synergistic effect, we have achieved high gene delivery efficiency toward hard-to-transfected BMSCs (~75.7%) seeded on the FG Ti surface. Not only that, the FG Ti-P/pDNA-6 implant exhibited antibacterial properties for better osteointegration, with an inhibition rate of up to 90% against *E.coli* and 80% against *S.aureus*. This antibacterial performance is attributed to reduced adherence and disrupted bacterial structure. Combined with the therapeutic gene, the FG Ti-P/pBMP2 implant significantly accelerated the healing process of bone defect, showing closely aligned bone tissues around the implants even in the third week after surgery in a rat model of femoral condylar defects. The design philosophy emphasizes the significance of achieving a harmonious equilibrium between chemical and mechanical regulation in the field of implant-dependent gene therapy. By combining the biocompatible DAM system and favorable fibrous topology, we aim to optimize the overall therapeutic outcome and promote successful bone regeneration.

Supplementary data

Supplementary data are available at *Regenerative Biomaterials* online.

Acknowledgments

The authors would like to thank Prof. Qiang Wei of Sichuan University for providing an experimental platform for real-time live cell imaging systems and VASE. We also extend our sincerest gratitude to engineers Jiao Lu and Guolong Meng of Sichuan University for their invaluable assistance in laser confocal, SEM and AFM imaging.

Funding

This work was financially supported by the National Natural Science Foundation of China (NSFC, No. 81873921 and 82372027), the Sino-German Cooperation Group Project (GZ1512), Science and Technology Project in Sichuan Province (2023YFH0060), Chengdu Science and Technology Program (2020-GH02-00007-HZ), Interdisciplinary innovation project from West China Hospital of Stomatology, Sichuan University (RD-03-202305), the Strategic Cooperation Project of Sichuan University-Luzhou City (2023CDLZ-11).

Conflicts of interest statement. The authors have declared that no competing interest exists.

References

1. Ma Z, Liu B, Li S, Wang X, Li J, Yang J, Tian S, Wu C, Zhao D. A novel biomimetic trabecular bone metal plate for bone repair and osseointegration. *Regener Biomater* **2023**;10:rbad003.
2. He Y, Yao M, Zhou J, Xie J, Liang C, Yin D, Huang S, Zhang Y, Peng F, Cheng S. $Mg(OH)_2$ nanosheets on Ti with immunomodulatory function for orthopedic applications. *Regener Biomater* **2022**;9:rbac027.
3. Guo C, Wu J, Zeng Y, Li H. Construction of 3D bioprinting of HAP/collagen scaffold in gelation bath for bone tissue engineering. *Regener Biomater* **2023**;10:rbad067.
4. Liu L, Wang J, Li Y, Liu B, Zhang W, Wang AW, Xu Q, Zhao B, Ma L. C. Laminin 332-functionalized coating to regulate the behavior of keratinocytes and gingival mesenchymal stem cells to enhance implant soft tissue sealing. *Regener Biomater* **2022**;9:rbac054.
5. Gan Q, Pan H, Zhang W, Yuan Y, Qian J, Liu C. Fabrication and evaluation of a BMP-2/dexamethasone co-loaded gelatin sponge scaffold for rapid bone regeneration. *Regener Biomater* **2022**;9:rbac008.
6. Raphel J, Karlsson J, Galli S, Wennerberg A, Lindsay C, Haugh MG, Pajarinen J, Goodman SB, Jimbo R, Andersson M, Heilshorn SC. Engineered protein coatings to improve the osseointegration of dental and orthopaedic implants. *Biomaterials* **2016**;83:269–82.
7. Wang Y, Feng Z, Liu X, Yang C, Gao R, Liu W, Ou-Yang W, Dong A, Zhang C, Huang P, Wang W. Titanium alloy composited with dual-cytokine releasing polysaccharide hydrogel to enhance osseointegration via osteogenic and macrophage polarization signaling pathways. *Regener Biomater* **2022**;9:rbac003.
8. Chen W, Li W, Xu K, Li M, Dai L, Shen X, Hu Y, Cai K. Functionalizing titanium surface with PAMAM dendrimer and human BMP2 gene via layer-by-layer assembly for enhanced osteogenesis. *J Biomed Mater Res A* **2018**;106:706–17.
9. Luo X, Meng C, Zhang Y, Du Q, Hou C, Qiang H, Liu K, Lv Z, Li J, Liu F. MicroRNA-21a-5p-modified macrophage exosomes as natural nanocarriers promote bone regeneration by targeting GATA2. *Regener Biomater* **2023**;10:rbad075.
10. Geng Z, Li Z, Cui Z, Wang J, Yang X, Liu C. Novel bionic topography with MiR-21 coating for improving bone-implant integration through regulating cell adhesion and angiogenesis. *Nano Lett* **2020**;20:7716–21.
11. Zhang L, Wu K, Song W, Xu H, An R, Zhao L, Liu B, Zhang Y. Chitosan/siCkip-1 biofunctionalized titanium implant for improved osseointegration in the osteoporotic condition. *Sci Rep* **2015**;5:10860.
12. Wang Z, Zhang J, Hu J, Yang G. Gene-activated titanium implants for gene delivery to enhance osseointegration. *Biomater Adv* **2022**;143:213176.
13. Liu W, Yu M, Chen F, Wang L, Ye C, Chen Q, Zhu Q, Xie D, Shao M, Yang L. A novel delivery nanobiotechnology: engineered miR-181b exosomes improved osteointegration by regulating macrophage polarization. *J Nanobiotechnol* **2021**;19:269.
14. Song W, Song X, Yang C, Gao S, Klausen LH, Zhang Y, Dong M, Kjems J. Chitosan/siRNA functionalized titanium surface via a layer-by-layer approach for in vitro sustained gene silencing and osteogenic promotion. *Int J Nanomed* **2015**;10:2335–46.
15. Chen L, Bai M, Du R, Wang H, Deng Y, Xiao A, Gan X. The non-viral vectors and main methods of loading siRNA onto the titanium implants and their application. *J Biomater Sci Polym Ed* **2020**;31:2152–68.
16. Li J, Liu X, Tao W, Li Y, Du Y, Zhang S. Micropatterned composite membrane guides oriented cell growth and vascularization for accelerating wound healing. *Regener Biomater* **2022**;10:rbac108.
17. Cao D, Ding J. Recent advances in regenerative biomaterials. *Regener Biomater* **2022**;9:rbac098.
18. Zhang Y, Wang X, Li Y, Liang J, Jiang P, Huang Q, Yang Y, Duan H, Dong X, Rui G, Lin C. Cell osteogenic bioactivity mediated precisely by varying scaled micro-pits on ordered micro/nano hierarchical structures of titanium. *Regener Biomater* **2022**;9:rbac046.

19. Wang Y, Wang N, Yang Y, Chen Y, Zhang Z. Cellular nanomechanics derived from pattern-dependent focal adhesion and cytoskeleton to balance gene transfection of malignant osteosarcoma. *J Nanobiotechnol* **2022**;20:499.
20. Yang Y, Wang X, Hu X, Kawazoe N, Yang Y, Chen G. Influence of cell morphology on mesenchymal stem cell transfection. *ACS Appl Mater Interfaces* **2019**;11:1932–41.
21. Chang R, Yan Q, Kingshott P, Tsai W-B, Wang P-Y. Harnessing the perinuclear actin cap (pnAC) to influence nanocarrier trafficking and gene transfection efficiency in skeletal myoblasts using nanopillars. *Acta Biomater* **2020**;111:221–31.
22. Wang S, Wu Z, Wang Y, Hong H, Zhang L, Chen Z, Zhang P, Chen Z, Zhang W, Zheng S, Li Q, Li W, Li X, Qiu H, Chen J. A homogeneous dopamine–silver nanocomposite coating: striking a balance between the antibacterial ability and cytocompatibility of dental implants. *Regener Biomater* **2022**;10:rbac082.
23. Tan J, Ren L, Xie K, Wang L, Jiang W, Guo Y, Hao Y. Functionalized TiCu/TiCuN coating promotes osteoporotic fracture healing by upregulating the Wnt/β-catenin pathway. *Regener Biomater* **2022**;10:rbac092.
24. Xue Y, Zhang L, Liu F, Dai F, Kong L, Ma D, Han Y. Alkaline "nanoswords" coordinate ferroptosis-like bacterial death for antibiosis and osseointegration. *ACS Nano* **2023**;17:2711–24.
25. Li J, Tan L, Liu X, Cui Z, Yang X, Yeung KWK, Chu PK, Wu S. Balancing Bacteria-Osteoblast competition through selective physical puncture and biofunctionalization of ZnO/polydopamine/arginine-glycine-aspartic acid-cysteine nanorods. *ACS Nano* **2017**;11:11250–63.
26. Wang R, Wang M, Jin R, Wang Y, Yi M, Li Q, Li J, Zhang K, Sun C, Nie Y, Huang C, Mikos AG, Zhang X. High strength titanium with fibrous grain for advanced bone regeneration. *Adv Sci* **2023**;10:e2207698.
27. Zhang J, Zhai B, Gao J, Li Z, Zheng Y, Ma M, Li Y, Zhang K, Guo Y, Shi X, Liu B, Gao G, Sun L. Plain metallic biomaterials: opportunities and challenges. *Regener Biomater* **2022**;10:rbac093.
28. Gu J, Su Y, Liu P, Li P, Yang P. An environmentally benign antimicrobial coating based on a protein supramolecular assembly. *ACS Appl Mater Interfaces* **2017**;9:198–210.
29. Chen X, Yang J, Liang H, Jiang Q, Ke B, Nie Y. Disulfide modified self-assembly of lipopeptides with arginine-rich periphery achieve excellent gene transfection efficiency at relatively low nitrogen to phosphorus ratios. *J Mater Chem B* **2017**;5:1482–97.
30. Wei Y, He T, Bi Q, Yang H, Hu X, Jin R, Liang H, Zhu Y, Tong R, Nie Y. A cationic lipid with advanced membrane fusion performance for pDNA and mRNA delivery. *J Mater Chem B* **2023**;11:2095–107.
31. Qi R, Zhang N, Zhang P, Zhao H, Liu J, Cui J, Xiang J, Han Y, Wang S, Wang Y. Gemini peptide amphiphiles with broad-spectrum antimicrobial activity and potent antibiofilm capacity. *ACS Appl Mater Interfaces* **2020**;12:17220–9.
32. Bai Z, Hu K, Shou Z, Yu J, Meng H, Zhou H, Chen L, Yu T, Lu R, Li N, Chen C. Layer-by-layer assembly of procyanidin and collagen promotes mesenchymal stem cell proliferation and osteogenic differentiation in vitro and in vivo. *Regener Biomater* **2022**;10:rbac107.
33. Decher G. Fuzzy nanoassemblies: toward layered polymeric multicomposites. *Science* **1997**;277:1232–7.
34. Wang D, Ha Y, Gu J, Li Q, Zhang L, Yang P. 2D protein supramolecular nanofilm with exceptionally large area and emergent functions. *Adv Mater* **2016**;28:7414–23.
35. Liu K, Yang C-M, Yang B-M, Zhang L, Huang W-C, Ouyang X-P, Qi F-G, Zhao N, Bian F-G. Directed self-assembly of vertical PS-b-PMMA nanodomains grown on multilayered polyelectrolyte films. *Chin J Polym Sci* **2019**;38:92–9.
36. Li X, Xu K, He Y, Tao B, Li K, Lin C, Hu J, Wu J, Wu Y, Liu S, Liu P, Wang H, Cai K. ROS-responsive hydrogel coating modified titanium promotes vascularization and osteointegration of bone defects by orchestrating immunomodulation. *Biomaterials* **2022**;287:121683.
37. Azzam F, Chaunier L, Moreau C, Lourdin D, Bertoncini P, Cathala B. Relationship between young's modulus and film architecture in cellulose nanofibril-based multilayered thin films. *Langmuir* **2017**;33:4138–45.
38. Alotaibi HF, Al Thaher Y, Perni S, Prokopovich P. Role of processing parameters on surface and wetting properties controlling the behaviour of layer-by-layer coated nanoparticles. *J Colloid Interface Sci* **2018**;36:130–42.
39. Deniz M, Deligöz H. Flexible self-assembled polyelectrolyte thin films based on conjugated polymer: quartz crystal microbalance dissipation (QCM-D) and cyclic voltammetry analysis. *Colloids Surf A* **2019**;563:206–16.
40. Zhang Z, Zeng J, Groll J, Matsusaki M. Layer-by-layer assembly methods and their biomedical applications. *Biomater Sci* **2022**;10:4077–94.
41. Zhang H, Xie L, Deng J, Zhuang W, Luo R, Wang J, Huang N, Wang Y. Stability research on polydopamine and immobilized albumin on 316L stainless steel. *Regener Biomater* **2016**;3:277–84.
42. Atluri K, Lee J, Seabold D, Elangovan S, Salem AK. Gene-activated titanium surfaces promote in vitro osteogenesis. *Int J Oral Maxillofac Implants* **2017**;32:e83.
43. Yi B, Zhou B, Dai W, Lu X, Liu W. Soft nanofiber modified micropatterned substrates enhance native-like endothelium maturation via CXCR4/calcium-mediated actin cytoskeleton assembly. *Nano Res* **2023**;16:792–809.
44. Yang C, Colosi P, Hugelier S, Zabezhinsky D, Lakadamyali M, Svitkina T. Actin polymerization promotes invagination of flat clathrin-coated lattices in mammalian cells by pushing at lattice edges. *Nat Commun* **2022**;13:6127.
45. Chao W-T, Kunz J. Focal adhesion disassembly requires clathrin-dependent endocytosis of integrins. *FEBS Lett* **2009**;583:1337–43.
46. Raisin S, Belamie E, Morille M. Non-viral gene activated matrices for mesenchymal stem cells based tissue engineering of bone and cartilage. *Biomaterials* **2016**;104:223–37.
47. Huang N-C, Sieber M, Hsu S-H. Correlating cell transfectability and motility on materials with different physicochemical properties. *Acta Biomater* **2015**;28:55–63.
48. Wang X, Hu X, Kawazoe N, Yang Y, Chen G. Manipulating cell nanomechanics using micropatterns. *Adv Funct Mater* **2016**;26:7634–43.
49. Li J, Song J, Meng D, Yi Y, Zhang T, Shu Y, Wu X. Electrospun naringin-loaded microsphere/sucrose acetate isobutyrate system promotes macrophage polarization toward M2 and facilitates osteoporotic bone defect repair. *Regener Biomater* **2023**;10:rbad006.
50. Gu Z, Fan S, Kundu SC, Yao X, Zhang Y. Fiber diameters and parallel patterns: proliferation and osteogenesis of stem cells. *Regen Biomater* **2023**;10:rbad001.
51. Salhotra A, Shah HN, Levi B, Longaker MT. Mechanisms of bone development and repair. *Nat Rev Mol Cell Biol* **2020**;21:696–711.
52. Ren X, Hu Y, Chang L, Xu S, Mei X, Chen Z. Electrospinning of antibacterial and anti-inflammatory Ag@hesperidin core-shell nanoparticles into nanofibers used for promoting infected wound healing. *Regener Biomater* **2022**;9:rbac012.
53. Busscher HJ, van der Mei HC, Subbiahdoss G, Jutte PC, van den Dungen JJ, Zaat SA, Schultz MJ, Grainger DW. Biomaterial-

associated infection: locating the finish line in the race for the surface. *Sci Transl Med* **2012**;4:153rv10.

54. Xing H, Lu M, Yang T, Liu H, Sun Y, Zhao X, Xu H, Yang L, Ding P. Structure-function relationships of nonviral gene vectors: lessons from antimicrobial polymers. *Acta Biomater* **2019**;86:15–40.
55. Zhang W, Liu J, Yang K, Qu W, Liu K, Liu N, Gu B, Hu N, Chu JJ, Wang PK. H. Unique role of arginine in positively-charged surface for promotion of antibacterial and osteogenetic capabilities. *Adv Mater Interfaces* **2019**;6:1901414.
56. Zhu Y, Akhtar MU, Li B, Chou S, Shao C, Li J, Shan A. The design of cell-selective tryptophan and arginine-rich antimicrobial peptides by introducing hydrophilic uncharged residues. *Acta Biomater* **2022**;153:557–72.
57. Sutterlin HA, Shi H, May KL, Miguel A, Khare S, Huang KC, Silhavy TJ. Disruption of lipid homeostasis in the Gram-negative cell envelope activates a novel cell death pathway. *Proc Natl Acad Sci USA* **2016**;113:E1565–74.
58. Zamani E, Johnson TJ, Chatterjee S, Immethun C, Sarella A, Saha R, Dishari SK. Cationic π-conjugated polyelectrolyte shows antimicrobial activity by causing lipid loss and lowering elastic modulus of bacteria. *ACS Appl Mater Interfaces* **2020**;12:49346–61.
59. Wang Y, Corbitt TS, Jett SD, Tang Y, Schanze KS, Chi EY, Whitten DG. Direct visualization of bactericidal action of cationic conjugated polyelectrolytes and oligomers. *Langmuir* **2012**;28:65–70.